© 2023 Hefei Institutes of Physical Science, Chinese Academy of Sciences and IOP Publishing Printed in China and the UK

Plasma Sci. Technol. **25** (2023) 055402 (8pp) https://doi.org/10.1088/2058-6272/aca9a7

Numerical studies on the influences of gas temperature on atmospheric-pressure helium dielectric barrier discharge characteristics

Weigang HUO (霍伟刚), **Jingsong LIN** (林靖松), **Tanxue YU** (于潭学), **Yuxin WANG** (王玉新)* **and Hua ZHANG** (张华)

School of Physics and Electronic Technology, Liaoning Normal University, Dalian 116029, People's Republic of China

E-mail: yuxinwang108@163.com

Received 2 September 2022, revised 23 November 2022
Accepted for publication 7 December 2022
Published 21 February 2023

Abstract

A fast-rising gas temperature is due to frequent collisions of the heavy particles in an atmospheric-pressure dielectric barrier discharge. In this paper, a two-dimensional fluid model is applied to investigate the influences of rising gas temperature on an atmospheric-pressure helium dielectric barrier discharge. With the increase in the gas temperature, it is found that: (1) a helium discharge can evolve from the discharge column to a homogeneous discharge; (2) the breakdown time is in advance and the gas breakdown voltage decreases; (3) the spatial distribution evolution of the electron density is similar to that of the helium atom density. The most significant discrepancy between them is that the electron densities are high at some positions where the helium atom densities are nevertheless low. Furthermore, the radial reduced electric fields are obtained under different gas temperatures. The physical reasons for the gas temperature effects are discussed. The simulation results provide a better understanding of the roles of the radial reduced electric field and the heavy particle.

Keywords: gas temperature, electron density, helium atom density, radial reduced electric field

(Some figures may appear in colour only in the online journal)

1. Introduction

Atmospheric-pressure dielectric barrier discharges (DBDs) usually exhibit three different discharge modes: filamentary mode, homogeneous mode and self-organized regular-discharge pattern mode [1]. In practical applications, the non-uniform filamentary DBDs cause likely local ablation or perforation of dielectric material [2]. Homogeneous DBDs can overcome these defects [3]. Therefore, homogeneous DBDs have been paid attention to in recent years [4].

Numerical simulations and experiments have been carried out to investigate homogeneous DBDs at least once [5–8]. These papers show that DBD mode depends on many factors, such as the working gas, driving frequency, electrode voltage, electrode gap and dielectric layer structure [5–8]. However, reports are relatively rare regarding the role of gas temperature in mode transition. Compared to a low-pressure DBD, the collisions among the particles in an atmospheric-pressure DBD are more frequent [9]. Therefore, the gas temperature may play an important role in an atmospheric-pressure DBD mode transition. Various discharge modes, such as glow-like discharge, Townsend discharge and filamentary discharge, have been studied under different gas temperatures [10–12], but it is still not reported that the transition is from the discharge column to a homogeneous discharge by varying gas temperature, and the corresponding physical mechanisms have not been fully elucidated.

In this paper, a two-dimensional (2D) fluid model is applied to the research on the influences of gas temperature on the characteristics of an atmospheric-pressure helium DBD.

* Author to whom any correspondence should be addressed.

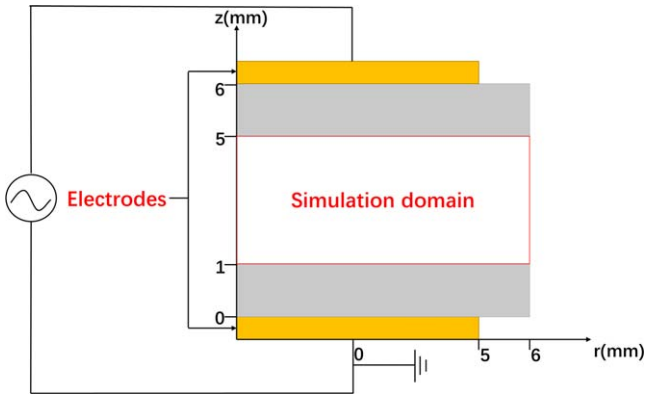

Figure 1. A schematic of the 2D fluid model.

To gain a better understanding of the mode transition with gas temperatures, we calculated the electron density, the helium atom density and the radial reduced electric field, etc, and gave the physical explanations.

2. Simulation model

A geometrical sketch of the 2D symmetric fluid model for this study is shown in figure 1. An atmospheric-pressure helium DBD is generated between two parallel metal plates, both of which are covered with thin uniform dielectric barrier layers. The upper electrode is driven by a sinusoidal alternating-current (AC) high-voltage power supply, and the lower electrode is grounded. The working gas is helium. In this simulation, six species (electron e, helium atom He, helium atom metastable He*, helium molecule metastable He_2^*, helium atom ion He^+ and helium molecule ion He_2^+) are used and 15 chemical reactions are employed (shown in table 1). Both the species and reactions are identical to those used in [13] and [14]. The rate coefficient data of those reactions are determined by the cross-section data [15]. The electron density and the electron energy density are obtained by solving the continuity equations with drift-diffusion approximation [16–19]:

$$\frac{\partial n_e}{\partial t} + \nabla \cdot \boldsymbol{\Gamma}_e = S_e \tag{1}$$

$$\boldsymbol{\Gamma}_e = -n_e \mu_e \boldsymbol{E} - D_e \nabla \cdot n_e \tag{2}$$

$$\frac{\partial n_\varepsilon}{\partial t} + \nabla \cdot \boldsymbol{\Gamma}_\varepsilon = -e\boldsymbol{\Gamma}_e \cdot \boldsymbol{E} - \sum_i \Delta E_i^e K_i - 3\frac{m_e}{m_{He}} K_B n_e \overline{\nu_e}(T_e - T_g) \tag{3}$$

$$\boldsymbol{\Gamma}_\varepsilon = -\frac{5}{3} n_\varepsilon \mu_e \boldsymbol{E} - \frac{5}{3} D_\varepsilon \cdot \nabla n_\varepsilon. \tag{4}$$

In formulas (1) and (2), n_e and $\boldsymbol{\Gamma}_e$ represent the electron number density and the electron flux vector; S_e is the sum of the source and loss items of the electron number density resulting from chemical reactions; μ_e and D_e represent the electron mobility and the electron diffusion coefficient, which are obtained with the Bolsig+solver [16]; and $\boldsymbol{E}$ is the local electric field vector.

In formulas (3) and (4), n_ε and $\boldsymbol{\Gamma}_\varepsilon$ represent the electron energy density and the electron energy flux vector, respectively. The three terms on the right-hand side of formula (3) represent the Joule heating and energy transfer due to inelastic and elastic collisions, respectively [18]. The ΔE_i^e and K_i are the energy loss during the inelastic collision process and the corresponding reaction rate (shown in table 1). Here, m_e and m_{He} refer to the masses of electrons and helium atoms or ions; K_B, T_g and T_e ($=\frac{2}{3}\overline{\varepsilon}$, $\overline{\varepsilon}$ is the initial average electron energy) indicate the Boltzmann constant, gas temperature and electron temperature, respectively; $\overline{\nu_e}$ is the momentum transfer rate between electrons and the background helium, which can also be obtained from the Bolsig+solver [18, 20, 21].

Because there are k kinds of heavy species in the reaction system, the transport properties are given by the following multi-component diffusion equations [16, 22, 23]:

$$\rho\frac{\partial w_k}{\partial t} = \nabla \cdot \boldsymbol{J}_k + S_k,\ k \in (1, 2, ..., Q) \tag{5}$$

$$\rho = M_n \frac{P}{RT_g} \tag{6}$$

$$\boldsymbol{J}_k = \rho w_k \boldsymbol{V}_k = \rho w_k \left(D_k \frac{\nabla w_k}{w_k} + D_k \frac{\nabla M_n}{M_n} - z_k \mu_k \boldsymbol{E} \right) \tag{7}$$

$$\mu_k = \frac{qD_k}{K_B T_g}. \tag{8}$$

In formula (5), ρ represents the mixture density; the subscript k represents the kth species; w represents the mass fraction of heavy species; $\boldsymbol{J}$ represents the heavy species diffusive flux; S is the heavy species source term; Q is the number of heavy species type.

In formula (6), M_n, P and R are the mean molar mass of the mixture, gas pressure and gas constant, respectively. Note that P in the gas gap is approximately constant due to a fixed initial gas pressure of 760.0 Torr.

In formula (7), D_k, z_k and μ_k are the diffusion coefficient, the charge number and the mobility of the kth heavy species, respectively. The diffusion coefficient (D_k) is the same as that in [24] and [25]. The mobility of the kth heavy species (μ_k) is calculated by formula (8). The background gas density is obtained by the following equation [16, 17]

$$w = 1 - \sum_{Q-1}^{k=1} w_k. \tag{9}$$

In addition, the local electric field E is obtained by solving Poisson's equation [16, 17],

$$\nabla \cdot (\varepsilon_0 \varepsilon_r \boldsymbol{E}) = -\nabla \cdot (\varepsilon_0 \varepsilon_r \nabla V) = \rho_V. \tag{10}$$

In formula (10), ε_0, ε_r, V and ρ_V are the vacuum permittivity, the relative permittivity, the electric potential and the space charge density, respectively.

The simulation parameters are chosen as follows: the discharge gap, the width of the electrode and the dielectric barrier layer are fixed to 4.0 mm, 10.0 mm and 12.0 mm, respectively. Both barrier layers are 1.0 mm thickness and the relative permittivity constant is set to 7.5. The gas pressure is 760.0 Torr. The secondary electron emission coefficient is assumed to be 0.01. For the initial charge balance over the

Table 1. Chemical reactions considered in the model. The units of the reaction rate coefficient for two body reactions and three body reactions are m^3/s and m^6/s. The units for T_e and n_e are eV and m^{-3}, respectively. Here, $f(\bar{\varepsilon}_0)$ represents the coefficient rate with the Maxwellian electron energy distribution.

No.	Reaction	Rate coefficient	Energy (eV)	References
1	$e + He \rightarrow e + He$	$f(\bar{\varepsilon}_0)$	/	[20]
2	$e + He \rightarrow e + He^*$	$f(\bar{\varepsilon}_0)$	19.82	[20]
3	$e + He \rightarrow 2e + He^+$	$f(\bar{\varepsilon}_0)$	25.60	[20]
4	$e + He^* \rightarrow 2e + He^+$	$f(\bar{\varepsilon}_0)$	4.78	[20]
5	$e + He^* \rightarrow e + He$	4.2×10^{-15}	−19.82	[28]
6	$e + He^+ \rightarrow He$	$1.327 \times 10^{-27} \times n_e \times T_e^{-4.4}$	−25.60	[29]
7	$e + He_2^+ \rightarrow He_2^*$	5×10^{-22}	−3.40	[30]
8	$e + He + He^+ \rightarrow He^* + He$	1×10^{-39}	0	[28]
9	$e + He_2^+ \rightarrow He^* + He$	$5.386 \times 10^{-13} \times T_e^{-0.5}$	0	[28]
10	$2e + He_2^+ \rightarrow He_2^* + e$	7.1×10^{-32}	0	[28]
11	$e + He_2^+ + He \rightarrow He_2^* + He$	5×10^{-39}	0	[31]
12	$e + He_2^* \rightarrow 2e + He_2^+$	$9.75 \times 10^{-16} \times T_e^{0.71} \times \exp(-3.4/T_e^{-4.4})$	3.40	[28]
13	$He^* + He^* \rightarrow e + He + He^+$	2.9×10^{-15}	/	[28]
14	$He^* + 2He \rightarrow He_2^* + He$	1.9×10^{-46}	/	[28]
15	$He^+ + 2He \rightarrow He + He_2^+$	6.3×10^{-44}	/	[28]

gap [17], the initial densities of uniform electrons, uniform He^+ and uniform He_2^+ are 1×10^{13} m^{-3}, 5×10^{12} m^{-3} and 5×10^{12} m^{-3}, respectively. The initial average electron energy is set to 5 eV [16, 22, 26], while the measured average electron energy is usually below 1 eV [27]. The initial time step of the solution was 1×10^{-13} s.

In this model, the boundary conditions are the same as those described in [14] and [17]. The accumulation of surface charges (including electron and heavy species) together with the quenching of excimers and the ion-induced secondary electron emission is considered on the symmetry axis and the solid surfaces between dielectrics and the gas gap. The boundary conditions for the heavy particle flux on the dielectric surfaces are as follows:

(i) Metastable species (He^*, He_2^*)

$$\boldsymbol{n} \cdot \boldsymbol{\Gamma}_m = \frac{\gamma_m}{1 - \gamma_m/2} \frac{1}{4} n_m \sqrt{\frac{8K_B T_g}{\pi M_m}} \tag{11}$$

where $\boldsymbol{n}$ and γ_m are the unit normal vector toward the surface and the sticking coefficient accounting for the occurring probability of the reaction. Here, $\boldsymbol{\Gamma}$, n and M are the flux term, density and mass respectively, and the subscript m indicates metastable species.

(ii) Ions (He^+, He_2^+)

$$\boldsymbol{n} \cdot \boldsymbol{\Gamma}_i = \frac{1}{4} n_i \sqrt{\frac{8K_B T_i}{\pi M_i}} + \alpha_s \mu_i n_i \boldsymbol{E} \tag{12}$$

where the subscript i indicates the ion, T_i refers to the ion temperature ($T_i \approx T_g$) and μ_i is the ion mobility coefficients. Here, α_s is a switching function, which is set to 1 if the drift velocity is directed toward the wall and to 0 otherwise [14, 19]. The electron flux and the electron energy flux on the dielectric surfaces are described in detail in [14, 17]. Some surface reactions are shown in table 2.

The above-mentioned equations (including the continuity equation, the multi-component diffusion equation, the Poisson equation and other equations associated with the boundary conditions, etc) are solved using multiphysics simulation software (COMSOL Multiphysics) [17] and the numerical results are obtained using the fast direct solver PARDISO provided by the COMSOL Multiphysics software. A superfine mesh method is utilized and the total number of degrees of freedom is 102515 in the calculation.

To evaluate the accuracy and applicability of this 2D fluid model, when the simulation parameters (voltage amplitude, voltage frequency, gas gap and relative dielectric permittivity, etc) are exactly the same as the experiment parameters in figure 2(a) of [33], the discharge current (I_{dis}) density, electrode voltage ($V_{appl)}$ and gas voltage (V_{gas}) are calculated using the above described 2D fluid model (see figure 2). When comparing figure 2 to figure 2(a) of [33], the simulation results (I_{dis} density peak value, I_{dis} density peak phase and gas breakdown voltage, etc) are almost the same as the presented experimental results in figure 2(a) of [33]. This means that the above described 2D fluid model can be used to study the characteristics of an atmospheric-pressure helium DBD.

3. Results and discussion

3.1. Effects of gas temperature on the spatial distribution of electron density

In the following simulations, both V_{appl} and the frequency are fixed at 2.0 kV and 20.0 kHz, respectively, and the gas temperature increases from 375.0 to 475.0 K (close to the gas temperature of atmospheric-pressure DBD [34]). When the steady state is reached, the electron density is averaged over one electrode voltage cycle, and then the spatial profiles of the

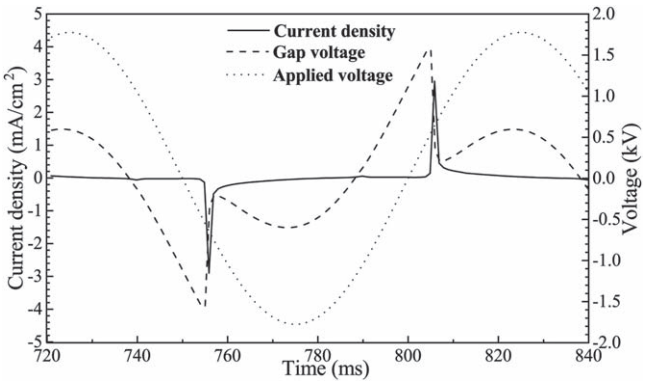

Figure 2. Time variation over one cycle of the calculated V_{appl}, V_{gas} and I_{dis} density when the steady state is reached. The simulation parameters were exactly the same as the experiment parameters in figure 2(a) of [33].

Table 2. Surface reactions considered in the model.

No.	Formula	Reaction probability	γ_i	Initial electron mean energy (eV)	References
1	$He^+ \rightarrow He$	1	0.01	2.50	[32]
2	$He_2^+ \rightarrow 2He$	1	0.01	2.50	[32]
3	$He^* \rightarrow 2He$	1	0	0	[32]
4	$He_2^* \rightarrow He$	1	0	0	[32]

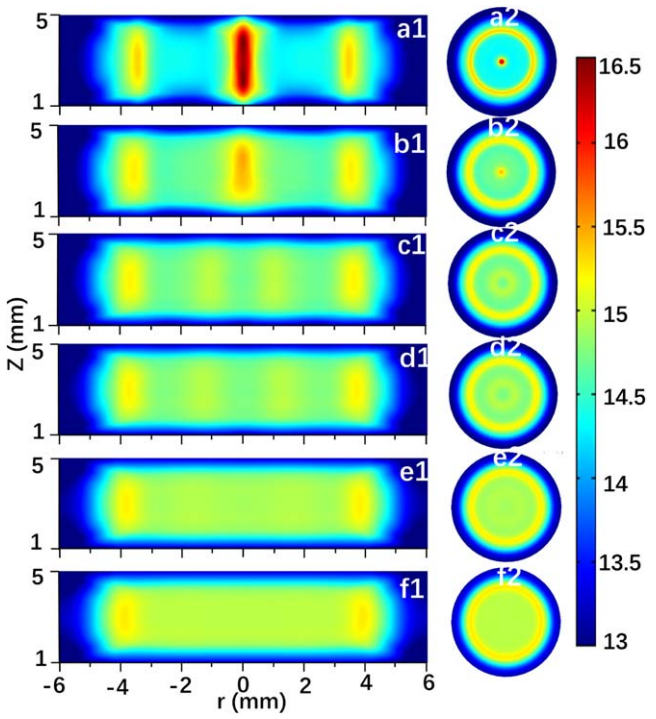

Figure 3. Spatial profiles of the time-averaged (the last cycle of the steady state) electron densities (in unit m^{-3}) under different gas temperatures: (a) 375.0 K, (b) 400.0 K, (c) 412.5 K, (d) 425.0 K, (e) 450.0 K and (f) 475.0 K. The front views are shown on the left side, while the top views are presented on the right side.

averaged electron density ($\log_{10}(n_e)$) are obtained under different gas temperatures (see figure 3).

For the discharge operated at the 375.0 K gas temperature, one local discharge column occurs at the electrode center, the other two occur symmetrically near the electrode edge (see figure 3(a1)) and a typical concentric-ring plasma discharge can be observed (see figure 3(a2)). The reason for this is that the electric field is stronger in the center of the overall discharge region and at the edge of the electrode than that in other positions [17]. The averaged electron densities between the central discharge column and the outer discharge columns (or outer discharge ring) are lower than those in the central discharge column or outer discharge ring. To facilitate the description, the region between the central discharge column and the outer discharge columns (or outer discharge ring) is defined as the weak discharge region. When the gas temperature is increased to 400.0 K, the outer discharge column (or discharge ring) width becomes broad and moves slightly toward the electrode edge, but the position of the central discharge column remains unchanged. In addition, the averaged electron densities increase in the weak discharge region but decrease in the central discharge column (see figures 3(b1) and (b2)).

With the further increase in the gas temperature to 412.5 K, the central discharge column disappears and two new discrete discharge columns (denoted as the inner discharge column hereafter) occur symmetrically around the position of the central discharge column (see figure 3(c1)), or a new ring plasma discharge is generated (see figure 3(c2)). The averaged electron densities decrease in the outer discharge columns but increase in the weak discharge region, which implies that the difference in the averaged electron density decreases between the discharge column and the weak discharge region and the discharge gradually becomes uniform (see figures 3(c1) and (c2)). As the gas temperature continues to rise, the inner discharge column gradually disappears (see figures 3(d2)–(f2)), mainly because the difference in the averaged electron density decreases further between the discharge column and the weak discharge region (see figures 3(d1) and (e1)), and the averaged electron density is almost uniform in the whole gas gap (see figure 3(f1)). The evolution of the averaged electron density shows that an atmospheric-pressure helium DBD can transit from the discharge column (or ring plasma discharge) at some local locations to a homogeneous discharge in the whole gas gap only by increasing the gas temperature. Some experimental results also show that a helium DBD can operate in different discharge modes, such as a homogeneous spot or the ring-like shape, by varying the gas temperature [11, 35, 36]. It is also worth noting that the evolution of an atmospheric-pressure helium DBD with the gas temperature is very similar to that of an atmospheric-pressure argon DBD with the applied voltage [17].

Figure 4 shows the spatial distribution of the degree of ionization ($=n_i/(n_i + n_a)$, where n_i and n_a are the ion and neutral particle densities, respectively) along the r direction under different gas temperatures. Note that: (1) only half of the spatial distribution of the degree of ionization is given due to the symmetric discharge geometry; (2) the degree of

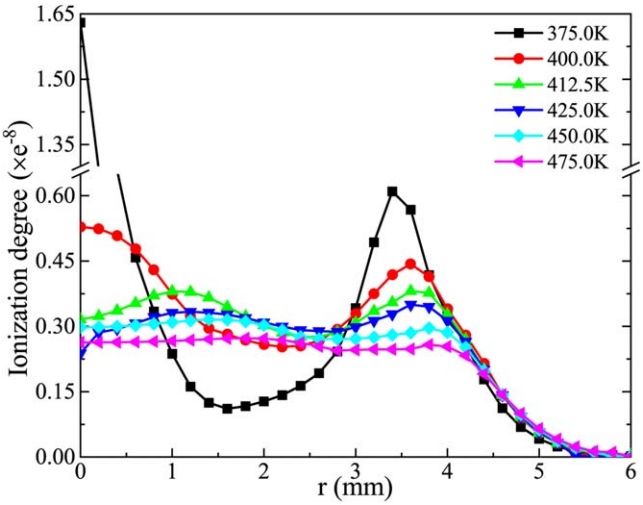

Figure 4. Spatial distributions of the degree of ionization along the r direction under different gas temperatures.

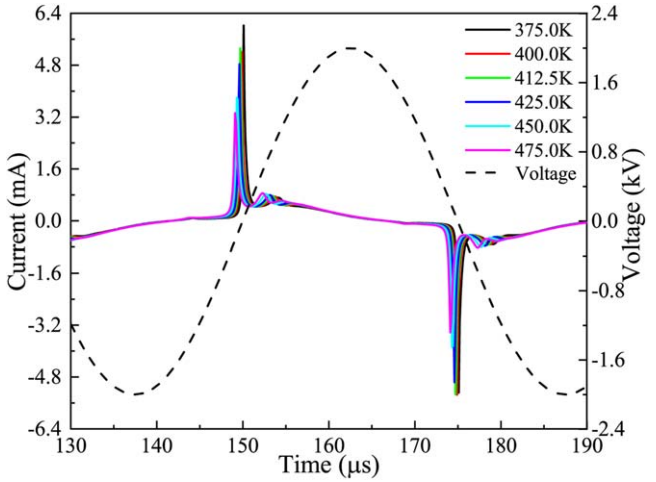

Figure 5. The V_{appl} and I_{dis} waveforms under different gas temperatures.

ionization in figure 4 is that at the absolute maximum of the discharge current. The influences of gas temperature on the discharge uniformity can also be clearly displayed in figure 4, which demonstrates that the spatial distribution of the degree of ionization has similar variation to the electron density (from non-uniform to uniform) along the r direction with the increment in the gas temperature. Specifically, the obtained curve of the degree of ionization versus r presents the maxima at lower gas temperature, and the number of and the position of the maximum degrees of ionization in figure 4 are exactly the same as those of the discharge columns in figure 3.

3.2. Influences of gas temperature on the electrical characteristics

For corona discharge between conventional needle-plate electrodes in air, the amplitude of the current pulse increases with the increasing ambient temperature [12], but the dependence of the current pulse on the gas temperature has not been studied when a plate-plate helium DBD transits from filamentary discharge to homogeneous discharge. Therefore, I_{dis}s are obtained under different gas temperatures (see figure 5). The most significant finding is that the current pulse amplitude decreases and the breakdown time advances when the gas temperature increases, which will result in the increase in the space charges in the discharge region and a decrease in the charges accumulated on the dielectric surface [17].

The electron density is averaged along the z direction, and the averaged electron density versus time is obtained under different gas temperatures (see figure 6). Note that different scales are used in figure 6 to better appreciate any changes. At the times about 150.0 ms and 175.0 ms (corresponding to the absolute maximum of the discharge current, respectively), two discharge channels occur around the positions $r = 0.0$ mm and $r = 3.5$ mm with maximal electron density of $2.74 \times 10^{17}\,\mathrm{cm}^{-3}$ at the gas temperature of 375.0 K. The positions of the two discharge channels are the same as those in figure 3(a1). With the increment in the gas temperature, the electron density corresponding to the maximum of the discharge current at the position $r = 0.0$ mm gradually decreases and gradually becomes the same as those at other positions, which implies that the discharge gradually becomes uniform.

Figure 7 shows the dependence of the gas gap breakdown voltage on gas temperature. More clearly, the gas gap breakdown voltage experiences a linear decrease when increasing the gas temperature. Han *et al* [37] verified experimentally that the breakdown voltage decreases as the gas temperature increases. One reason for the above feature is that the increase in the gas temperature will result in a decrease in the neutral gas density in the gap according to formula (6). As a result, the reduced electric field ($=E/n$, where n is the gas density) increases (see figure 8), which leads to the decrease in the gap breakdown voltage [38]. A uniform Townsend discharge is more easily obtained at lower gas gap breakdown voltages [39].

3.3. Discussion

It is well known that the gas temperature is dependent on the heavy particle temperature [40]. To obtain a deeper understanding of the dependence of helium DBD characteristics on gas temperature, the spatial profiles of the time-averaged helium atom densities ($\log_{10}(n_{\mathrm{e}})$) are studied under different gas temperatures, as shown in figure 9. Note that the helium atom density (the order of $10^{25}\,\mathrm{m}^{-3}$) is much greater than the other helium particle densities (the order of He_2^* $10^{19}\,\mathrm{m}^{-3}$, the order of He^* $10^{18}\,\mathrm{m}^{-3}$, the order of He_2^+ $10^{17}\,\mathrm{m}^{-3}$ and the order of He^+ $10^{16}\,\mathrm{m}^{-3}$); therefore, only the spatial profile of the time-averaged helium atom density is given. For the same reason as in figure 6, different scales are also used in figure 9.

The variation in figure 9 shows the following characteristics: when increasing the gas temperatures, the spatial distribution of the helium atom density varies from a concentric single ring (see figures 9(a1), (a2) and (b1), (b2)), a concentric double ring (see figures 9(c1), (c2) and (d1), (d2)) to homogeneous discharge in the whole gas gap (see

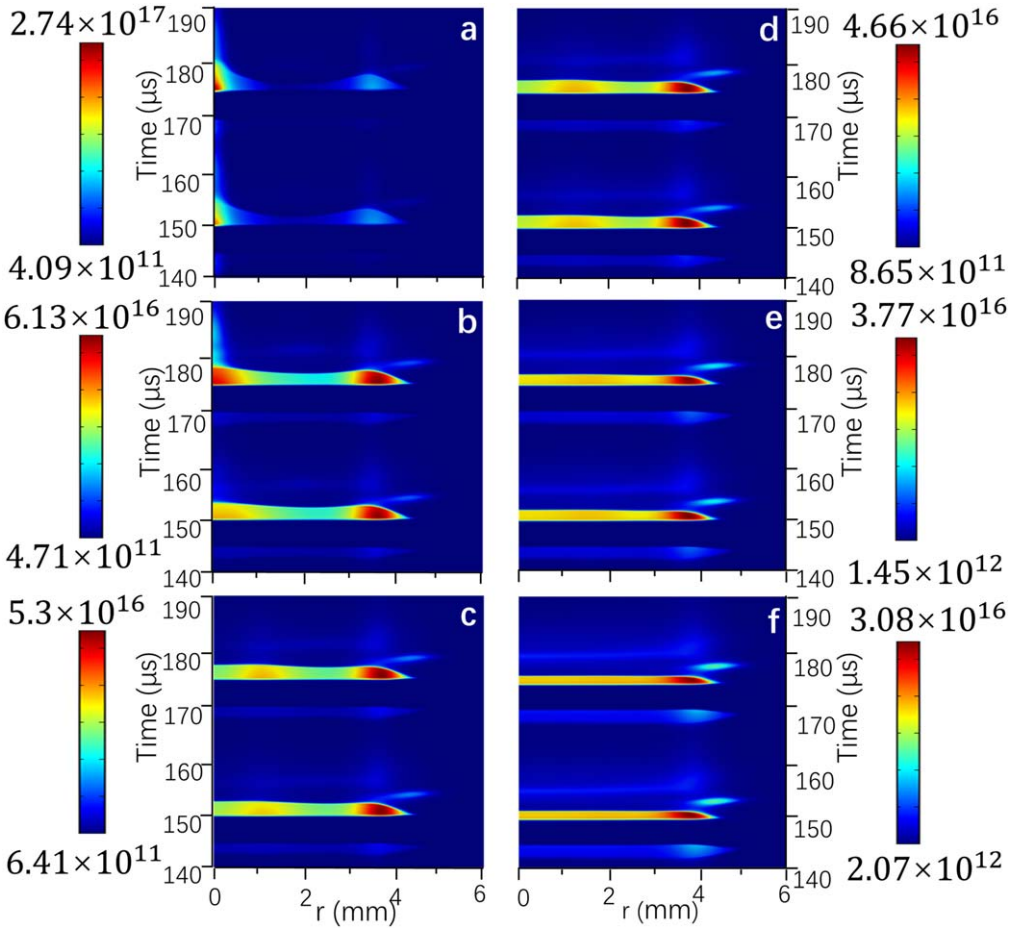

Figure 6. Temporal contour maps of the z axis averaged electron density (cm^{-3}) under different gas temperatures: (a) 375.0 K, (b) 400.0 K, (c) 412.5 K, (d) 425.0 K, (e) 450.0 K and (f) 475.0 K.

figures 9(e1), (e2) and (f1), (f2)). The differences shown in figures 3 and 9 are that: (1) the helium atom densities are low while the electron density is high at the same location; (2) the helium atom densities are low at the electrode edge or on the dielectric surface when the discharge operates in a nearly homogeneous mode, which implies that the local temperature is high; (3) the helium atom density differences at different positions are relatively small at the same temperature.

The reduced electric field is closely related to the gas density and is one of the key factors influencing the discharge uniformity. Therefore, figure 10 shows both the radial reduced electric field (denoted as E_{rr} hereafter) and the spatial profile of the electron density at the time about 150.0 ms (corresponding to the maximum of the discharge current). Note that the time corresponding to the maximum of the discharge current usually varies with the gas temperature (see figure 5). It can be clearly seen that the E_{rr} presents three minima at some radial positions, and the strong local E_{rr} are generated around the three minimum E_{rr} at the gas temperature of 375.0 K due to the faster drift of electrons than that of ions [41] (see figure 10(a1)). According to the direction of the E_{rr} (see figure 10 (a2)), the strong local E_{rr} can attract the electrons into the local discharge (called the 'electron-focusing effect', EFE) [42, 43]. This EFE can cause the formations of the local high electron density region and of the weak discharge region near the cathode region (see figure 10(a2)). Note that the arrows in figure 10(a2) are magnified ten times compared to others presented in figure 10.

When the gas temperature is increased to 400.0 K, the E_{rr} in the weak discharge region becomes wider and decreases [17] (see figure 10(b1)). This is because the average width of the low helium atom densities region increases (see figures 9(b1) and (b2)). Meanwhile, the space charges in the discharge region increase and the charges accumulated on the dielectric surface decrease due to the breakdown in advance [17] (see figure 5). The decrease in the E_{rr} will result in the decrement in the EFE [17, 41]. As a result, the electrons in the discharge column more easily spread to the edge of the discharge column or into the weak discharge region, which can cause the local discharge area near the cathode region to increase (see figure 10(b2)) or the width of the discharge column to broaden (see figure 3(b1)). It is worth noting that the outer discharge columns slightly move toward the electrode edge because the E_{rr} in the right (left) of the outer discharge column are stronger than those in the left (right) (see figure 10(b1)).

As the gas temperature is increased to 412.5 K, it is decreased in both the E_{rr} in the weak discharge region and the

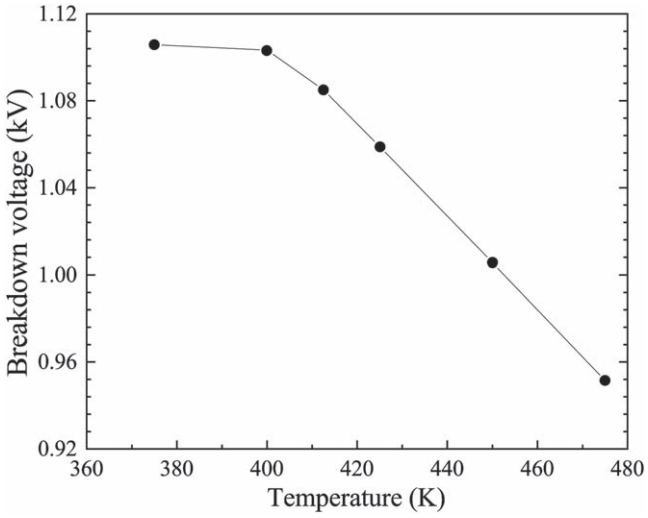

Figure 7. The gap breakdown voltage as a function of the gas temperature.

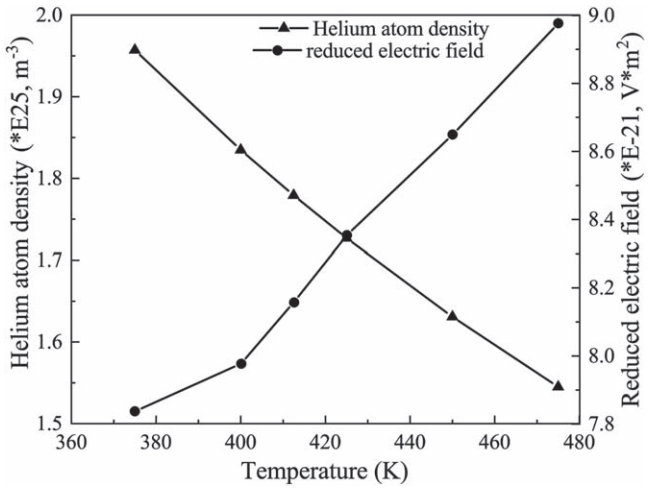

Figure 8. The spatial-temporal helium atom density (in unit m^{-3}) and reduced electric field as a function of gas temperature.

E_{rr} discrepancy between the weak discharge region and in the local discharge (see figure 10(c1)). This means the further decrement of the EFE will increase the electron density in the weak discharge region. Meanwhile, the gas breakdown voltage is lower than those at the gas temperature less than 412.5 K (see figure 7). As a result, more local discharges near the cathode region (see figure 10(c2)) or the ring plasma discharge in the gas gap (see figure 3(c2)) can occur at radial locations at the same V_{appl} where the electron density is high.

With the continuing increase in the gas temperature, the E_{rr} in the weak discharge region continues to decrease and the uniformity of the E_{rr} gradually increases (see figures 10(d1)–(f1)), implying that the EFE gradually disappears, and the electron density spatial distribution near the cathode region gradually becomes uniform (see figures 10(d2)–(f2)). When the gas temperature further increases to 475.0 K, many electron

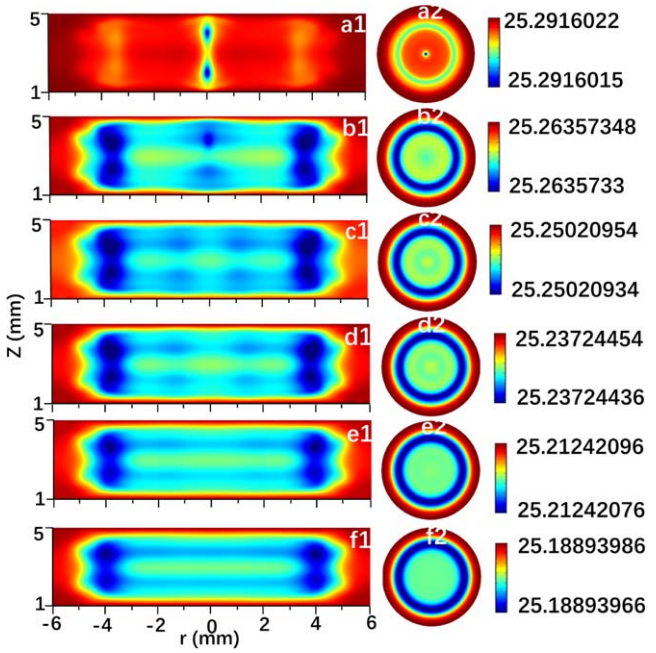

Figure 9. Spatial profiles of the time-averaged helium atom densities (in unit m^{-3}) under different gas temperatures. The gas temperatures in figures 9(a)–(f) correspond to those in figures 3(a)–(f), respectively. The front views are shown on the left side, while the top views are presented on the right side.

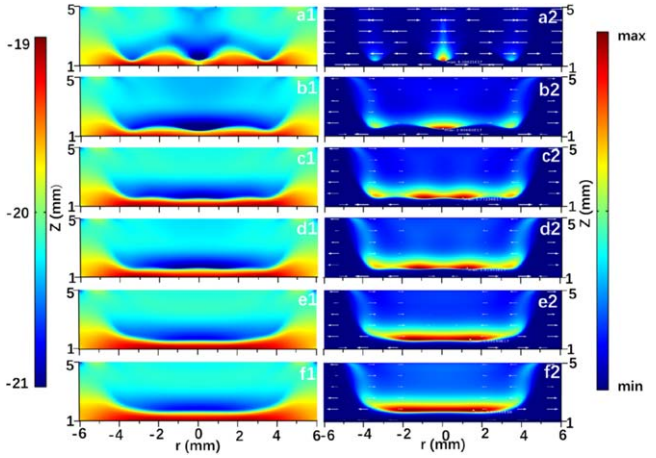

Figure 10. Spatial profiles of the radial reduced electric field (left) and the electron densities (right). The arrows in figures 10(b2)–(f2) indicate the direction of the radial reduced electric field. The gas temperatures in figures 10(a)–(f) correspond to those in figures 3(a)–(f), respectively.

avalanches can form simultaneously and a spatially uniform discharge can be initiated in the whole radial location (see figures 10(e2) and (f2) or figures 3(e1) and (f1)) due to more uniform distribution of electron density and the lower breakdown voltage [44]. In addition, the helium atom density near the dielectric surface is low and its distribution is uniform (see figure 9(f1)), causing the reduced electric field to become strong and uniform near the dielectric surface. As a result, a uniform discharge occurs near the dielectric surface (see figure 10(f2)).

4. Conclusions

In this paper, a 2D fluid model is used to study the influences of gas temperature on atmospheric-pressure helium DBD characteristics. The following important conclusions are drawn:

(1) An atmospheric-pressure helium DBD can evolve from a concentric single ring or a concentric double ring to homogeneous discharge by gradually increasing the gas temperature from 375.0 K to 475.0 K at a constant V_{appl}.
(2) Both the gas breakdown voltage and current pulse amplitude decrease, and the breakdown time advances with the increase in gas temperature.
(3) At the same gas temperature, the spatial distribution discrepancy between the electron density and the helium atom density is that the electron densities are high at some positions where the helium atom densities are nevertheless low. The physical reason for the above discrepancy is elucidated as follows. The discharge is strong in some local regions. It implies that the local electron density is high, which causes the local temperature to increase. As a result, the local helium atom density decreases.
(4) The E_{rr} in the discharge column region is much less than that in the weak discharge region, which contributes to the formation of some local discharge columns at the gas temperature of 375.0 K. With the increase in the gas temperature, the E_{rr} decreases in the weak discharge region but increases in the discharge column region; finally, the discrepancy between the E_{rr}s in the two regions completely disappears. As a result, the EFE gradually disappears and then a helium discharge column gradually transits to homogeneous discharge.

Acknowledgments

This research was supported by the Liaoning Provincial Department of Education Fund (No. LJ2020008).

References

[1] Kogelschatz U 2002 *IEEE Trans. Plasma Sci.* **30** 1400
[2] Wang Y H and Wang D Z 2003 *Acta Phys. Sin.* **52** 1694 (in Chinese)
[3] Bonnin X *et al* 2013 *Eur. Phys. J. Appl. Phys.* **64** 10901
[4] Fang Z *et al* 2007 *J. Phys. D: Appl. Phys.* **40** 1401
[5] Xu Y G *et al* 2017 *Phys. Plasmas* **24** 043507
[6] Ouyang J T *et al* 2018 *Plasma Sci. Technol.* **20** 103002
[7] Zhang S *et al* 2019 *Spectrochim. Acta A Mol. Biomol. Spectrosc.* **207** 294
[8] Laiadi A, Chentouf A and Laghmich Y 2020 *Mater. Today Proc.* **24** 160
[9] Ohno N *et al* 2006 *Plasma Fusion Res.* **1** 028
[10] Kang W S, Kim H S and Hong S H 2010 *IEEE Trans. Plasma Sci.* **38** 1982
[11] Noma Y *et al* 2008 *Appl. Phys. Express* **1** 046001
[12] Sun H Y *et al* 2017 *Phys. Plasmas* **24** 103506
[13] Zhang Y H *et al* 2018 *AIP Adv.* **8** 095327
[14] Zhang Y H *et al* 2019 *Plasma Sci. Technol.* **21** 074003
[15] IST-Lisbon database. LXCat program. [2022-12-1]. https://nl.lxcat.net/cache/638894af894f6/
[16] Zhang Y H *et al* 2019 *Plasma Sources Sci. Technol.* **28** 075003
[17] Wan J *et al* 2019 *Phys. Plasmas* **26** 103510
[18] Zhang X F *et al* 2014 *Appl. Therm. Eng.* **72** 82
[19] Jiang Y Y *et al* 2022 *Plasma Sci. Technol.* **24** 054003
[20] Hagelaar G J M and Pitchford L C 2005 *Plasma Sources Sci. Technol.* **14** 722
[21] BOLSIG+Electron Boltzmann equation solver. [2005] http://bolsig.laplace.univ-tlse.fr/BOLSIG+Electron Boltzmann equation solver. [2005] http://www.bolsig.laplace.univ-tlse.fr/index.html
[22] Lazarou C *et al* 2016 *Plasma Sources Sci. Technol.* **25** 055023
[23] Lieberman M A and Lichtenberg A J 2005 *Principles of Plasma Discharges and Materials Processing* 2nd edn (Hoboken: Wiley-Interscience)
[24] Ellis H W *et al* 1976 *At. Data Nucl. Data Tables* **17** 177
[25] Ellis H W *et al* 1984 *At. Data Nucl. Data Tables* **31** 113
[26] Wang L J, Zheng Y S and Jia S L 2016 *Phys. Plasmas* **23** 103504
[27] Boisvert J S *et al* 2018 *Plasma Sources Sci. Technol.* **27** 035005
[28] Kong M G and Deng X T 2003 *IEEE Trans. Plasma Sci.* **31** 7
[29] Park G *et al* 2008 *Plasma Process. Polym.* **5** 569
[30] Yuan X H and Raja L L 2003 *IEEE Trans. Plasma Sci.* **31** 495
[31] Wang Y H and Wang D Z 2005 *Phys. Plasmas* **12** 023503
[32] Zhang Y H, Ning W J and Dai D 2018 *AIP Adv.* **8** 035008
[33] Mangolini L *et al* 2004 *J. Phys. D: Appl. Phys.* **37** 1021
[34] Shi J J and Kong M G 2007 *Appl. Phys. Lett.* **90** 101502
[35] Choi J H *et al* 2008 *Appl. Phys. Lett.* **93** 081504
[36] Chen Y F *et al* 2020 *Plasma Sci. Technol.* **22** 055404
[37] Uhm H S, Jung S J and Kim H S 2003 *J. Korean Phys. Soc.* **42** S989
[38] Huo W G *et al* 2014 *Phys. Plasmas* **21** 053505
[39] Raizer Y P 1991 *Gas Discharge Physics* (Berlin: Springer)
[40] Chinnov V F *et al* 2018 *High Temp.* **56** 25
[41] Li B *et al* 2018 *J. Phys. D: Appl. Phys.* **51** 015203
[42] Li B and Ouyang J T 2016 *Phys. Plasmas* **23** 113509
[43] Qiao Y J, Li B and Ouyang J T 2016 *Phys. Plasmas* **23** 013510
[44] Levatter J I and Lin S C 1980 *J. Appl. Phys.* **51** 210